Thermoelectric properties of the tetrahedrite–tennantite solid solutions Cu12Sb4–xAsxS13 and Cu10Co2Sb4–yAsyS13 ($0 \leq x, y \leq 4$)

Petr Levinský, Christophe Candolfi, Anne Dauscher, Janusz Tobola, Jiří Hejtmánek, Bertrand Lenoir

Thermoelectric properties of the tetrahedrite-tennantite solid solutions $Cu_{12}Sb_{4-x}As_xS_{13}$ and $Cu_{10}Co_2Sb_{4-y}As_yS_{13}$ ($0 \leq x, y \leq 4$)

Petr Levinsky[1,2,3], Christophe Candolfi[1], Anne Dauscher[1], Janusz Tobola[4], Jiří Hejtmánek[2], Bertrand Lenoir[1,*]

[1]*Institut Jean Lamour, UMR 7198 CNRS – Université de Lorraine, Campus ARTEM, 2 allée André Guinier, BP 50840, 54011 Nancy, France*

[2]*Institute of Physics of the Czech Academy of Sciences, Prague, Czech Republic*

[3]*Faculty of Nuclear Sciences and Physical Engineering, Czech Technical University, Prague, Czech Republic*

[4]*Faculty of Physics and Applied Computer Science, AGH University of Science and Technology, 30-059 Krakow, Poland*

[*]Contact author: bertrand.lenoir@univ-lorraine.fr

Abstract

Tetrahedrites, a class of copper- and sulfur-rich minerals, exhibit inherently very low lattice thermal conductivity and adjustable electronic properties that make them interesting candidates for thermoelectric applications. Here, we investigate the influence of isovalent As substitution on the Sb site on the structural and transport properties (5 – 700 K) of the two solid solutions $Cu_{12}Sb_{4-x}As_xS_{13}$ and $Cu_{10}Co_2Sb_{4-y}As_yS_{13}$ ($0 \leq (x,y) \leq 4$). Electronic band structure calculations predict that As has only a weak influence on the valence bands and hence, on the *p*-type metallic character of $Cu_{12}Sb_4S_{13}$. In agreement with these predictions, all the samples of the series

$Cu_{12}Sb_{4-x}As_xS_{13}$ exhibit *p*-type metallic behavior with relatively low electrical resistivity and moderate thermopower values that only slightly evolve with the As content. In contrast, the substitution of Co for Cu in As-rich samples seems less favorable as suggested by a decrease in the Co concentration with increasing the As content. This trend leads to a concomitant increase in the electrical resistivity and thermopower leaving the *ZT* values practically unchanged with respect to purely Cu-based samples. As a result, peak *ZT* values ranging between 0.60 and 0.75 are achieved at 700 K for both series. The lack of significant variations in the *ZT* values confirms the robustness of the thermoelectric performances of tetrahedrites with respect to variations in the Sb-to-As ratio.

Introduction

Tetrahedrites are a class of natural sulfur-based minerals mined worldwide that constitute an abundant source of copper and silver. The relationships between their chemical compositions and geographical location have been the subject of numerous investigations in mineralogy and geology. Recently, the electric and thermal properties of both synthetic and natural tetrahedrites have been investigated in more detail evidencing semiconducting electronic properties combined with extremely low lattice thermal conductivity akin to that seen in amorphous compounds.[1-20] Both characteristics qualify these compounds as possible thermoelectric materials that enable solid-state conversion of heat into electricity and vice versa. The conversion efficiency at an absolute temperature *T* directly depends on the transport properties of the materials via the dimensionless thermoelectric figure of merit *ZT* defined as $ZT = \alpha^2 T/\rho\kappa$ where α is the thermopower, ρ is the electrical resistivity and κ is the total thermal conductivity.[21,22]

Over the last years, a growing number of studies were focused on the optimization of the thermoelectric properties of the ternary tetrahedrite $Cu_{12}Sb_4S_{13}$ through various substitutions on the Cu, Sb or S sites.[1-23] Efforts were also devoted to the possibility to minimize the cost and time of the synthesis process by mixing natural ore with synthetic materials, via solvothermal synthesis or using alternative synthesis techniques such as melt-spinning or high-energy ball milling.[3,26-28] Depending on the nature and concentration of the substituting species, the *p*-type metallic state of $Cu_{12}Sb_4S_{13}$ is driven towards a heavily-doped semiconducting state before eventually entering a semiconducting regime when two electrons per chemical formula are added.[1-23] Most of these substitutions lead to enhanced thermoelectric performances with *ZT* values ranging between 0.7 and 1.0 around 700 K for optimized compositions.[1-23] On a more fundamental side, the intrinsic ability of tetrahedrites to impede heat transport has been shown to be tied to the peculiar chemical environment of some of the Cu atoms of the cubic crystal structure (Figure 1).[8,11,29] These atoms, referred to as Cu2, are located in a slightly-distorted trigonal planar coordination and exhibit strong, anisotropic thermal displacements towards the active lone pair electrons of Sb atoms located on either side.[8,11] These lone pairs are believed to play an essential role in creating the anharmonic potential felt by the Cu2 atoms and thus, in lowering the lattice thermal conductivity.

While most of the reported studies have dealt with substitutions on the Cu site, only substitutions of Te and Bi for Sb have been considered so far.[12,13,30] While Bi has a significantly lower solubility limit (up to $x = 0.16$ compared to $x = 2.1$ for Te when considering the chemical formulas $Cu_{12}Sb_{4-x}Bi_xS_{13}$ and $Cu_{12}Sb_{4-x}Te_xS_{13}$, respectively) and an overall detrimental influence on the *ZT* values with respect to $Cu_{12}Sb_4S_{13}$,[30] the substitution of Te for Sb was found to mirror that of various transition metals with an increase in both the thermopower and electrical resistivity as a result of the decreased hole concentration.[12,13] Hence, enhanced *ZT* values could be achieved with a maximum *ZT* of 0.85 at 700 K for $x = 1$.[12,13]

In contrast to these two elements, a complete solid solution exists between the tetrahedrite $Cu_{12}Sb_4S_{13}$ and the isostructural compound $Cu_{12}As_4S_{13}$ named tennantite. Recently, Tanaka *et al.*[31] explored the influence of external pressure and As substitution on the metal-insulator transition accompanied by a cubic-to-tetragonal distortion near 85 K in $Cu_{12}Sb_4S_{13}$ by means of low-temperature magnetic susceptibility and electrical resistivity measurements. However, no detailed investigation on the influence of substitution of As for Sb on the thermoelectric properties of $Cu_{12}Sb_4S_{13}$ has been reported so far. The interest of studying this substitution is reinforced by the possibility to prepare tetrahedrites with enhanced thermoelectric properties from a mixture of their natural and synthetic variants.[3] Depending on the location where the natural tetrahedrite was mined, the mineral ore can be either Sb-rich or As-rich. It is thus important to determine to which extent the Sb-to-As ration of the chosen mineral will influence the thermoelectric properties of the final compound.

Here, we report on the synthesis, crystal structure and thermoelectric properties measured in a broad temperature range (5 – 723 K) of the two systems, $Cu_{12}Sb_{4-x}As_xS_{13}$ and $Cu_{10}Co_2Sb_{4-y}As_yS_{13}$, across the entire solid-solution range ($0 \leq x,y \leq 4$). These two series have been considered in order to contrast the influence of the isovalent As substitution on compounds exhibiting either metallic ($Cu_{12}Sb_4S_{13}$) or semiconducting ($Cu_{10}Co_2Sb_4S_{13}$) behavior. The experimental results are complemented by electronic band structure calculations, performed within the KKR-CPA framework, of the electronic density of states and the dispersion curves for the two end-member compounds ($x = 0$ and 4) of the series $Cu_{12}Sb_{4-x}As_xS_{13}$.

Experimental and theoretical sections

Synthesis

Polycrystalline samples of $Cu_{12}Sb_{4-x}As_xS_{13}$ and $Cu_{10}Co_2Sb_{4-y}As_yS_{13}$ with $x = y = 0$, 1, 2, 3 and 4 were synthesized by powder metallurgy. Stoichiometric amounts of elemental Cu (99.99%, powders), Co (99.998%, powders), Sb (99.999%, shots), As (99.999%, powders) and S (99.999%, powders) were sealed under secondary vacuum in quartz tubes. The sealed tubes were slowly heated up to 923 K at a rate of 0.3 K min^{-1}, dwelt at that temperature for 12 hours and cooled to room temperature at a rate of 0.5 K min^{-1}. The ingots were ground into fine powders and cold-pressed into cylindrical pellets, which were further annealed at 723 K for 6 days to improve the chemical homogeneity. After quenching in room-temperature water, the annealed pellets were powdered again and densified by spark plasma sintering (SPS) for 4 min under 80 MPa at 773 K for the Co-containing samples. For the Co-free samples, the sintering temperature was varied between 723 K for Sb-rich compositions and 798 K for As-rich compositions. All the cylindrical pellets showed an experimental density, determined by weight and geometrical dimensions, higher than 97% of the theoretical density.

Structural and Chemical Characterizations

The crystal structure was determined by powder X-ray diffraction (PXRD) at 300 K ($CuK\alpha_1$ radiation, λ = 1.54056 Å) using a Bruker D8 Advance diffractometer. The room-temperature lattice parameters were determined by Rietveld refinements using the Fullprof software.[32] The chemical homogeneity of the samples was assessed by scanning electron microscopy (SEM) in backscattering mode and energy dispersive X-ray spectroscopy (EDXS)

using a Quanta FEG650 (FEI). The actual chemical compositions were determined by electron probe microanalysis (EPMA) using a Cameca SX 100 instrument. $CuFeS_2$, Co, Sb_2S_3, GaAs and $CuFeS_2$ were used as standards to determine the Cu, Co, Sb, As and S concentrations, respectively. These measurements were performed on mirror-polished surfaces using < 0.1μm colloidal silica (OP-S). The actual chemical compositions, listed in Table 1, were determined by averaging between 50 and 60 spots measured on each sample and by normalizing to 29 atoms per formula unit.

Transport Properties Measurements

At low temperatures (5 – 300 K), the electrical resistivity, thermopower and total thermal conductivity were measured simultaneously via the static four-probe method using a home-made instrument described in detail elsewhere.[33] In order to correct the radiation losses that accompany these measurements above 150 K, the instrument was calibrated using various materials exhibiting low thermal conductivity values such as acrylic glass or polystyrene. The measurements were realized on bar-shaped samples cut from the SPS pellets with a diamond wire saw (typical dimensions of 2.5×2×8 mm^3). Four silver leads were attached onto the samples with a small amount of conductive silver paint.

The thermopower and the electrical resistivity were measured simultaneously between 300 and 700 K with a ZEM-3 apparatus (Ulvac-Riko) on bar-shaped samples of typical dimensions 2.5×2.5×7 mm^3. Thermal diffusivity a was measured by a laser flash technique (Netzsch LFA 427) on disc-shaped samples (10 mm diameter, 0.9 mm thickness). The thermal conductivity was calculated by the relation $\kappa = aC_p d$ where d is the experimental density and C_p is the isobaric specific heat. As a first approximation, C_p was estimated following the Dulong-Petit law $C_p = 3NR$ where N is the number of atoms per chemical formula and R is the

gas constant. The density was considered temperature-independent in the present case. The combined experimental uncertainty on the *ZT* values between 300 and 700 K is estimated to be ~17%.[34]

Electronic Band Structure Calculations

The electronic densities of states (DOS) of $Cu_{12}Sb_{4-x}As_xS_{13}$ for x = 0, 1, 2, 3 and 4 were calculated using the Korringa-Kohn-Rostoker (KKR) method with the coherent potential approximation (CPA) that enables to treat explicitly the chemical disorder induced by As substitution on the Sb site.[35,36] In these calculations, the local density approximation (LDA) parameterization of Perdew and Wang was employed for the exchange-correlation part.[37] The position of the Fermi level was determined accurately by the generalized Lloyd formula.[38] For all compositions, the experimental lattice parameters (Table 1) and atomic coordinates determined from Rietveld refinements against the PXRD data were used. For well-converged crystal potential and atomic charges (below 1 mRy and $10^{-3}e$, respectively), the total-, site- and orbital-decomposed DOS were computed using a tetrahedron method for integration in the reciprocal *k*-space.[38] For x = 0 and 4, the complex energy dispersion curves were calculated in the first *bcc* Brillouin zone along high-symmetry directions. In the case of the two end-member compounds $Cu_{12}Sb_4S_{13}$ and $Cu_{12}As_4S_{13}$, their electronic structure was also calculated using the full-potential KKR method, which allows for a direct comparison with the KKR-CPA results obtained within the spherical crystal potential of the muffin-tin form.

Results and discussion

Electronic band structure

Figure 2 shows the dispersion curves for the two end-member compounds $Cu_{12}Sb_4S_{13}$ and $Cu_{12}As_4S_{13}$. As reported in our prior study,[12] the dispersion relations $E(k)$ of $Cu_{12}Sb_4S_{13}$ are characterized by weakly dispersive valence bands along the G–H, N–H and N–P directions and by an indirect energy gap of ~1.4 eV. These non-parabolic bands result in high effective masses of holes. The Fermi level lies inside the valence bands, confirming the *p*-type metallic character of this compound.

Because the top of the valence bands and their evolution with x mainly govern the transport properties, Figure 3 shows magnifications of the zone in the vicinity of the Fermi level for the disordered $Cu_{12}Sb_{4-x}As_xS_{13}$ alloys. Figure 4 presents the electronic density of states (DOS) of the $Cu_{12}Sb_4S_{13}$ and $Cu_{12}As_4S_{13}$ ordered compounds in the whole energy range. At first glance, one notices that the energy gap appearing above the 116th band (corresponding to systems such as $Cu_{12}Sb_2Te_2S_{13}$ or $Cu_{10}Sb_4S_{13}$ possessing 232 valence electrons *i.e.* 12×11[Cu] + 2×5[Sb] + 2×6[Te] + 13×6[S]) is one of the main characteristics of the electronic structure of both tetrahedrite and tennantite compounds.[2,8,12] In this regard, and assuming that the electronic band structure is sufficiently 'rigid', the Fermi level (possessing 230 valence electrons, 12×11[Cu] + 4×5[Sb/As] + 13×6[S]) is expected to be host by the valence bands in all the $Cu_{12}Sb_{4-x}As_xS_{13}$ compounds, leaving two unoccupied holes per chemical formula up to the valence states edge. Indeed, E_F is located ~ 0.1 eV (in average) below the band gap edge in view of our electronic structure calculations. The electronic DOS of these alloys consists essentially of *d*-Cu and *p*-S states (*s*-S states are located at the lowest energy), with some admixture of *p*-Sb/As states. These last states, however, contribute more significantly to the

bottom of the conduction bands than in the valence bands. A comparison of the electronic structure of $Cu_{12}Sb_4S_{13}$ and $Cu_{12}As_4S_{13}$ in the whole energy range (Figures 4) reveals that the substitution of isoelectronic As for Sb, leading to a contraction of the unit cell, not only results in a shrinkage of the energy gap but also in the overall broadening of the valence bands. This expected behavior is clearly seen in the modification of the relative position of the *s* states of the S2 atoms, which are shifted towards lower energy in $Cu_{12}As_4S_{13}$ and form nearly separate DOS peak, unlike the case of $Cu_{12}Sb_4S_{13}$, where these states are joined by upper-lying valence states.

Keeping in mind the LDA limits in the calculation of the energy band gap as well as the fact that E_F is located at finite DOS, our KKR computations show an important reduction of the band gap value with respect to $Cu_{12}Sb_4S_{13}$ (~ 1.4 eV) and $Cu_{12}As_4S_{13}$ (~ 0.9 eV). Our results obtained for the end-member compounds are well supported by the KKR-CPA calculations of $Cu_{12}Sb_{4-x}As_xS_{13}$ alloys, which show a smooth decrease in the band gap energy with increasing *x*. Interestingly, the apparently different *p*-states of Sb and As lying in the lower energy range of conduction states play a predominant role in the band gap evolution, since the main part of *p*-As states have systematically lower energy and are larger than the corresponding *p*-Sb states in this energy range. Such behavior seems to be related to more attractive crystal potential of As with respect to that of Sb in $Cu_{12}Sb_{4-x}As_xS_{13}$, which is supported by the KKR-CPA calculations of electron charges around these atoms showing that 0.3 additional electron remains inside the muffin-tin sphere of As than inside the same volume around Sb atoms. Moreover, it is worth noting that, in spite of the monotonous band gap decrease in $Cu_{12}Sb_{4-x}As_xS_{13}$ with increasing *x*, the electronic DOS shape near E_F is not affected by As substitution. The Fermi level is located near the DOS peak constituted mostly by *d*-Cu and *p*-S states, regardless of the investigated alloy composition. These theoretical results suggest that the *p*-

type transport properties of $Cu_{12}Sb_4S_{13}$ should be only weakly affected by substituting As for Sb.

Crystal structure and phase analysis

Figures 5a and 5b show the PXRD patterns of the Co-free and Co-containing series of samples. For both series, all the main reflections can be indexed to the $I\bar{4}3m$ space group of tetrahedrites with only small fractions of secondary phases indicating that solid solutions are indeed formed. For the $Cu_{12}Sb_{4-x}As_xS_{13}$ series, these phases were identified as the famatinite-luzonite solid solution ($Cu_3(Sb,As)S_4$ crystallizing in a tetragonal structure) for the x = 0, 1 and 2 samples and enargite (orthorhombic Cu_3AsS_4) for the x = 3 and 4 samples. In the Co-containing series, a small amount of a pyrite analogue CoS_2 could be detected in the y = 2, 3 and 4 samples and of the ternary $CuCo_2S_4$ in the y = 0 and 1 samples. Given the low concentration of these secondary phases, their presence is not expected to significantly affect the measured transport properties presented in the next part. Moreover, the substitution of As for Sb in $Cu_{12}Sb_4S_{13}$ suppresses the exsolution process undergone by this compound below 373 K, as observed for other substitutions.[1-23]

The lattice parameters were inferred from Rietveld refinements against the PXRD data (see Table 1) including the secondary phases observed in the PXRD patterns. In agreement with the results obtained by Tanaka *et al.*[31] on the $Cu_{12}Sb_{4-x}As_xS_{13}$ series (Figure 5c), the lattice parameter decreases linearly with the As content following a Vegard's law. The lattice parameters of the Co-containing samples are slightly higher than those in the other series due to the presence of Co that expands the cubic unit cell of the $Cu_{12}(Sb,As)_4S_{13}$ tetrahedrite.[10] The lattice parameters determined for the As-free samples are in good agreement with those obtained in prior studies.[10,31]

SEM-EDX analyses confirmed the nature of the secondary phases determined by PXRD and also revealed the presence of minute amounts of $CuSbS_2$. Elemental X-ray mappings showed an overall homogeneous distribution of the elements within the tetrahedrite matrix. EPMA measurements carried out on the Co-free series are consistent with the PXRD and SEM results indicating a good correlation between the nominal and actual compositions (see Table 1). In contrast, the analyses performed on the Co-containing series reveal a decrease in the Co content as the As concentration increases. These results suggest that the substitution of Co for Cu becomes less favorable in the presence of As which might be due to the contraction of the unit cell with increasing the As content.

Transport properties

Figures 6a and 6b show the temperature dependence of the electrical resistivity for both series of compounds. All the samples of the $Cu_{12}Sb_{4-x}As_xS_{13}$ series are metallic with electrical resistivity values that slightly increase with increasing temperature between 300 and 700 K. For $Cu_{12}Sb_4S_{13}$, the steep rise observed below 85 K corresponds to a metal-to-insulator transition accompanied by displacements of the S2 and Cu2 atoms without symmetry reduction.[39] In agreement with the results of Tanaka *et al.*[31], the marked increase in ρ is strongly lessened upon substituting As for Sb. However, the increase in ρ is never fully suppressed suggesting that some remnant of this transition might still be present in substituted samples. The presence of As only weakly influences the *p*-type metallic nature of $Cu_{12}Sb_4S_{13}$ with ρ values varying only between 9 and 11 $\mu\Omega$.m at 300 K.

As observed in the previous series, the substitution of As for Sb in semiconducting $Cu_{10}Co_2Sb_4S_{13}$ does not significantly alter its low-temperature behavior (Figure 6b). ρ rapidly rises by several orders of magnitude upon cooling below 100 K suggesting that the samples

enter a hopping-like regime of electrical conduction. This regime is followed by a weak temperature dependence of the electrical resistivity up to 700 K. The variations of ρ with the As content are mainly driven by the decrease in the Co concentration with increasing *y* as determined by EPMA measurements.

Without any exception, all the tetrahedrites studied so far show *p*-type electrical conduction in agreement with electronic band structure calculations. The present two series of samples follow this general trend with positive thermopower values over the entire temperature range (Figures 7a and 7b). The fact that all samples of the $Cu_{12}Sb_{4-x}As_xS_{13}$ series behave as degenerate semiconductors is in agreement with the moderate thermopower values measured and with our calculations. The absence of metal-to-insulator transition in the As-substituted samples is further evidenced by the linear variation observed near 85 K that contrasts with the abrupt change in $\alpha(T)$ at this temperature in $Cu_{12}Sb_4S_{13}$. Regardless of the chemical composition, the monotonous increase in α with *T* above 300 K is consistent with the diffusive nature expected in degenerate systems. At 700 K, the maximum α values vary between 120 and 130 $\mu V\ K^{-1}$.

The non-linear temperature dependence of $\alpha(T)$ observed for the Co-containing samples is consistent with their semiconducting nature. The variations in the α values with *y* faithfully reflect the trend observed in $\rho(T)$ with the most resistive samples exhibiting the highest α values. The decrease in α with increasing the As content is a direct consequence of the concomitant decrease in the Co concentration which increases the degeneracy of the hole gas synonymous with lower α values.

The temperature dependence of the total thermal conductivity κ of the $Cu_{12}Sb_{4-x}As_xS_{13}$ and $Cu_{10}Co_2Sb_{4-y}As_yS_{13}$ series is shown in Figures 8a and 8b. Common to both series of samples, the presence of As has no influence on the glass-like thermal conductivity exhibited by these tetrahedrites. The absence of pronounced dielectric maximum at low temperatures is

tied to the low-energy optical modes associated with the anisotropic thermal displacement of the Cu2 atoms that results in active Umklapp scattering.[8] The anomaly seen near 85 K for the x = 0 sample, that corresponds to a metal-to-insulator transition observed in the $\rho(T)$ data,[1,39] does not entirely disappear upon substituting As for Sb. Shallow dips are still observable below 100 K in the x = 1, 2 and 3 samples, the temperature near which an increase in the ρ data is observed, pointing to a common origin of both features. Intriguingly, a more pronounced step-like anomaly is clearly observed below 150 K for the x = 4 sample. Measurements of the specific heat in this temperature region by Tanaka *et al*.[31] evidenced a peak at 124 K whose shape and amplitude is different from those observed for lower As contents. Unlike $Cu_{12}Sb_4S_{13}$, our results evidence that this peak is not associated with any significant anomaly in the thermopower data, further showing that this transition is not accompanied by a metal-to-insulator crossover. These differences indicate that the tennantite $Cu_{12}As_4S_{13}$ experiences a low-temperature phase transition distinct from that of the tetrahedrite $Cu_{12}Sb_4S_{13}$. Further low-temperature diffraction experiments are necessary to determine whether the transition in the As substituted samples is related to a structural distortion or a phase separation, that is, an exsolution process.

The higher κ values measured for the $Cu_{12}Sb_{4-x}As_xS_{13}$ series compared to $Cu_{10}Co_2Sb_{4-y}As_yS_{13}$ are due to the larger contribution of holes to the heat transport. This electronic contribution κ_e has been estimated using the Wiedemann-Franz law $\kappa_e = LT/\rho$, where L is the Lorenz number (see Figure 8). The temperature dependence of L has been determined by considering a single-parabolic band model assuming acoustic phonon scattering as the main scattering mechanism of holes (see Figures S1 and S2 in the Electronic Supplementary Information file). The lattice thermal conductivity values κ_L, obtained by subtracting κ_e from κ (Figures 8a and 8b), are very low in both series, on the order of 0.5 W m^{-1} K^{-1} above 300 K, and only slightly vary upon warming to 700 K. The κ_L values are close to the glassy limit of 0.5 W m^{-1} K^{-1} estimated by measurements of the transverse and longitudinal sound velocities.[12]

The fact that the estimated κ_L values for the $Cu_{12}Sb_{4-x}As_xS_{13}$ series are lower than the predicted minimum thermal conductivity is likely due to an overestimation of L, suggesting some deviations from a simple single-parabolic band behavior in these metallic tetrahedrites. The nearly equivalent κ_L values across the entire two series indicate that the substitution of As for Sb does not enhance point defect scattering that usually further lowers the thermal transport in solid solutions.

The weak influence of As on the transport properties of $Cu_{12}Sb_4S_{13}$ and $Cu_{10}Co_2Sb_4S_{13}$ is reflected by the temperature dependence of the *ZT* values shown in Figure 9. A peak *ZT* value of 0.75 was achieved at 700 K in both series of samples. This value remains similar in As-containing samples when considering the experimental uncertainty in the determination of *ZT*.

Conclusion

The tetrahedrite-tennantite solid solutions $Cu_{12}Sb_{4-x}As_xS_{13}$ and $Cu_{10}Co_2Sb_{4-y}As_yS_{13}$ have been successfully synthesized for $0 \leq x,y \leq 4$. In agreement with electronic band structure calculations, the presence of As does not change the *p*-type metallic character of $Cu_{12}Sb_4S_{13}$ and the semiconducting nature of $Cu_{10}Co_2Sb_4S_{13}$. Our chemical analyses revealed that As and Co tend to compete when simultaneously present, leading to a decrease in the Co concentration when the As content increases. The very low lattice thermal conductivity values remain similar regardless of the chemical composition (~ 0.5 W m^{-1} K^{-1} at 700 K) indicating the absence of significant alloying effects. As a result, As substitution yields similar *ZT* values that reach 0.75 at 700 K. Our results show that As has neither a beneficial nor a detrimental influence on the thermoelectric properties of tetrahedrites. More importantly, given the fact that natural specimens often possess both Sb and As in their chemical composition, the thermoelectric

properties obtained in mixtures of natural and synthetic tetrahedrites should be rather insensitive to the Sb-to-As ratio initially present in the mineral.

Acknowledgements

The authors acknowledge the financial support from the French National Agency (ANR) in the frame of the project MASSCOTE ("Matériaux sulfures à structures complexes: application à la thermoélectricité", project identifier ANR-15-CE05-0027). This work was performed with the financial support of the Grant Agency of the Czech Republic (Project No. 18-12761S) and the Operational Program Research, Development and Education (Center of Advanced Applied Sciences project No. CZ.02.1.01/0.0/0.0/16_019/0000778). J. T. was partially supported by the AGH UST statutory tasks (No. 11.11.220.01/5) from the Polish Ministry of Science and Higher Education. P. L. acknowledges the financial support of the French Ministry of Foreign Affairs.

References

1 K. Suekuni, K. Tsuruta, T. Ariga and M. Koyano, *Appl. Phys. Express*, 2012, **5**, 051201.

2 X. Lu, D. T. Morelli, Y. Xia, F. Zhou, V. Ozolins, H. Chi, X. Zhou and C. Uher, *Adv. Energy Mater.*, 2013, **3**, 342-348.

3 X. Lu and D. T. Morelli, *Phys. Chem. Chem. Phys.*, 2013, **15**, 5762-5766.

4 K. Suekuni, K. Tsuruta, M. Kunii, H. Nishiate, E. Nishibori, S. Maki, M. Ohta, A. Yamamoto and M. Koyano, *J. Appl. Phys.*, 2013, **113**, 043712.

5 J. Heo, G. Laurita, S. Muir, M. A. Subramanian and D.A. Keszler, *Chem. Mater.*, 2014, **26**, 2047-2052.

6 R. Chetty, D. S. Prem Kumar, G. Rogl, P. Rogl, E. Bauer, H. Michor, S. Suwas, S. Puchegger, G. Giester and R. C. Mallik, *Phys. Chem. Chem. Phys.*, 2015, **17**, 1716-1727.

7 T. Barbier, P. Lemoine, S. Gascoin, O. I. Lebedev, A. Kaltzoglou, P. Vaqueiro, A. V. Powell, R.I. Smith and E. Guilmeau, *J. Alloys Compd.*, 2015, **634**, 253-262.

8 Y. Bouyrie, C. Candolfi, S. Pailhès, M. M. Koza, B. Malaman, A. Dauscher, J. Tobola, O. Boisron, L. Saviot and B. Lenoir, *Phys. Chem. Chem. Phys.*, 2015, **17**, 19751-19758.

9 E. Lara-Curzio, A. F. May, O. Delaire, M. A. McGuire, X. Lu, C.-Y. Liu, E. D. Case and D. T. Morelli, *J. Appl. Phys.*, 2014, **115**, 193515.

10 R. Chetty, A. Bali, M. H. Naik, G. Rogl, P. Rogl, M. Jain, S. Suwas and R. C. Mallik, *Acta Mater.*, 2015, **100**, 266-274.

11 W. Lai, Y. Wang, D. T. Morelli and X. Lu, *Adv. Funct. Mater.*, 2015, **25**, 3648-3657.

12 Y. Bouyrie, C. Candolfi, V. Ohorodniichuk, B. Malaman, A. Dauscher, J. Tobola and B. Lenoir, *J. Mater. Chem. C*, 2015, **3**, 10476-10487.

13 X. Lu and D. T. Morelli, *J. Elec. Mater.*, 2014, **43**, 1983.

14 X. Lu, D. T. Morelli, Y. Xia and V. Ozolins, *Chem. Mater.*, 2015, **27**, 408-413.

15 Y. Bouyrie, C. Candolfi, J.-B. Vaney, A. Dauscher and B. Lenoir, *J. Elec. Mater.*, 2016, **45**, 1601-1605.

16 Y. Bouyrie, C. Candolfi, A. Dauscher, B. Malaman and B. Lenoir, *Chem. Mater.*, 2015, **27**, 8354-8361.

17 Y. Bouyrie, S. Sassi, C. Candolfi, J-B. Vaney, A. Dauscher and B. Lenoir, *Dalton Trans.*, 2016, **45**, 7294-7302.

18 X. Lu, D. T. Morelli, Y. Wang, W. Lai, Y. Xia and V. Ozolins, *Chem. Mater.*, 2016, **28**, 1781-1786.

19 Y. Kosaka, K. Suekuni, K. Hashikuni, Y. Bouyrie, M. Ohta, T. Takabatake, *Phys. Chem. Chem. Phys.* **19**, 8874-8879 (2017).

20 D. S. Prem Kumar, R. Chetty, P. Rogl, G. Rogl, E. Bauer, P. Malar, R. C. Mallik, *Intermetallics* **78**, 21-29 (2016).

21 P. Vaqueiro, G. Guélou, A. Kaltzoglou, R. I. Smith, T. Barbier, E. Guilmeau, A.V. Powell, *Chem. Mater.* **29**, 4080-4090 (2017).

22 Y. Yan, H. Wu, X. Lu, X. Zhou, *Ener. Stor. Mater.* **13**, 127-133 (2018).

23 D. P. Weller, G. E. Kunkel, A. M. Ochs, D. T. Morelli, M. E. Anderson, *Mater. Today Phys.* **7**, 1-6 (2018).

24 H. J. Goldsmid, in *Thermoelectric Refrigeration*, Temple Press Books, Ltd., London, 1964.

25 *Thermoelectrics and its Energy Harvesting*, ed. D. M. Rowe, CRC Press, 2012.

26 D. J. James, X. Lu, D. T. Morelli and S. L. Brock, *ACS Appl. Mater. Interfaces*, 2015, **7**, 23623-23632.

27 T. Barbier, S. Rollin-Martinet, P. Lemoine, F. Gascoin, A. Kaltzoglou, P. Vaqueiro, A. V. Powell and E. Guilmeau, *J. Am. Ceram. Soc.*, 2015, **99**, 51-56.

28 A. P. Gonçalves, E. B. Lopes, J. Monnier, J. Bourgon, J.-B. Vaney, A. Piarristeguy, A. Pradel, B. Lenoir, G. Delaizir, M. F. C. Pereira, E. Alleno and C. Godart, *J. Alloys Compd.*,

2016, **664**, 209-217.

29 A. F. May, O. Delaire, J. L. Niedziela, E. Lara-Curzio, M. A. Susner, D. L. Abernathy, M. Kirkham and M. A. McGuire, *Phys. Rev. B: Condens. Matter Mater.*, 2016, **93**, 064104.

30 D. S. Prem Kumar, R. Chetty, O. E. Femi, K. Chattopadhyay, P. Malar and R. C. Mallik, *J. Elec. Mater.*, 2017, **46**, 2616-2622.

31 H. I. Tanaka, K. Suekuni, K. Umeo, T. Nagasaki, H. Sato, G. Kutluk, E. Nishibori, H. Kasai and T. Takabatake, *J. Phys. Soc. Jpn.*, 2016, **85**, 014703.

32 J. Rodriguez-Carvajal, *Physica B*, 1993, **192**, 55-69.

33 J. Hejtmánek, Z. Jirák, M. Maryško, C. Martin, A. Maignan, M. Hervieu and B. Raveau, *Phys. Rev. B*, 1999, **60**, 14057.

34 E. Alleno, D. Bérardan, C. Byl, C. Candolfi, R. Daou, R. Decourt, E. Guilmeau, S. Hébert, J. Hejtmanek, B. Lenoir, P. Masschelein, V. Ohorodniichuk, M. Pollet, S. Populoh, D. Ravot, O. Rouleau and M. Soulier, *Rev. Sci. Instrum.*, 2015, **86**, 011301.

35 A. Bansil, S. Kaprzyk, P. E. Mijnarends and J. Tobola, *Phys. Rev. B: Condens. Matter Mater.* Phys., 1999, **60**, 13396.

36 T. Stopa, S. Kaprzyk and J. Tobola, *J. Phys.: Condens. Matter*, 2004, **16**, 4921.

37 J. P. Perdew and Y. Wang, *Phys. Rev. B: Condens. Matter Mater. Phys.*, 1992, **45**, 13244.

38 S. Kaprzyk and A. Bansil, *Phys. Rev. B: Condens. Matter Mater. Phys.*, 1990, **42**, 7358.

39 D. I. Nasonova, V. Yu. Verchenko, A. A. Tsirlin and A. V. Shevelkov, *Chem. Mater.*, 2016, **28**, 6621-6627.

Table Captions

Table 1. Lattice parameters inferred from Rietveld refinements against the PXRD data and actual chemical compositions of the samples measured by EPMA for the series $Cu_{12}Sb_{4-x}As_xS_{13}$ and $Cu_{10}Co_2Sb_{4-y}As_yS_{13}$. All the chemical compositions were normalized to 29 atoms per formula unit.

Nominal composition	*Actual composition*	*a (Å)*
$Cu_{12}Sb_4S_{13}$	$Cu_{11.98}Sb_{4.10}S_{12.92}$	10.318(7)
$Cu_{12}Sb_3AsS_{13}$	$Cu_{12.10}Sb_{3.03}As_{0.98}S_{12.89}$	10.282(1)
$Cu_{12}Sb_2As_2S_{13}$	$Cu_{11.95}Sb_{2.01}As_{2.05}S_{12.99}$	10.243(7)
$Cu_{12}SbAs_3S_{13}$	$Cu_{11.94}Sb_{0.98}As_{3.12}S_{12.97}$	10.205(7)
$Cu_{12}As_4S_{13}$	$Cu_{11.94}As_{4.24}S_{12.81}$	10.163(7)
$Cu_{10}Co_2Sb_4S_{13}$	$Cu_{10.22}Co_{1.80}Sb_{4.06}S_{12.91}$	10.342(9)
$Cu_{10}Co_2Sb_3AsS_{13}$	$Cu_{10.48}Co_{1.64}Sb_{3.11}As_{0.91}S_{12.86}$	10.304(4)
$Cu_{10}Co_2Sb_2As_2S_{13}$	$Cu_{10.21}Co_{1.68}Sb_{2.04}As_{1.96}S_{12.89}$	10.256(5)
$Cu_{10}Co_2SbAs_3S_{13}$	$Cu_{10.24}Co_{1.72}Sb_{1.07}As_{3.08}S_{12.90}$	10.221(3)
$Cu_{10}Co_2As_4S_{13}$	$Cu_{10.60}Co_{1.36}As_{4.22}S_{12.82}$	10.178(1)

Figure Captions

Fig. 1 Perspective view of the cubic unit cell of the tetrahedrite $Cu_{12}Sb_4S_{13}$ in ellipsoid representation (95% probability level). Cu1, Cu2, Sb/As, S1 and S2 atoms are represented by dark blue, green, brown, yellow and red ellipsoids, respectively.

Fig. 2 Dispersion curves along high symmetry directions in the Brillouin zone for $x = 0$ and $x = 4$ calculated by the KKR method. In both panels, the Fermi level has been arbitrarily set to 0 eV.

Fig. 3 Magnification around the Fermi level of the total and partial densities of states for the series $Cu_{12}Sb_{4-x}As_xS_{13}$ ($x = 0$, 1, 2 and 4) calculated by the KKR-CPA method. In all panels, the Fermi level has been arbitrarily set to 0 eV.

Fig. 4 Partial densities of states in the whole energy range for the $x = 0$ and 4 compounds calculated by the KKR-CPA method. For sake of clarity, the total DOS is not shown. In both panels, the Fermi level has been arbitrarily set to 0 eV.

Fig. 5 PXRD patterns of the a) $Cu_{12}Sb_{4-x}As_xS_{13}$ and b) $Cu_{10}Co_2Sb_{4-y}As_yS_{13}$ series. The insets show the shift of the main diffraction peak as the As concentration increases. In each panel, the reflections of the secondary phases are marked by symbols. The symbols >, v, * and # mark the reflections of the secondary phases identified as famatinite-luzonite (tetragonal $Cu_3(Sb,As)S_4$), enargite (Cu_3AsS_4), $CuCo_2S_4$ and CoS_2, respectively. c) Variation in the lattice parameter *a* as a function of the As content *x*.

Fig. 6 Temperature dependence of the electrical resistivity of the a) $Cu_{12}Sb_{4-x}As_xS_{13}$ and b) $Cu_{10}Co_2Sb_{4-y}As_yS_{13}$ series.

Fig. 7 Thermopower as a function of temperature for the a) $Cu_{12}Sb_{4-x}As_xS_{13}$ and b) $Cu_{10}Co_2Sb_{4-y}As_yS_{13}$ series.

Fig. 8 Temperature dependence of the total, lattice and electronic thermal conductivities of the series a) $Cu_{12}Sb_{4-x}As_xS_{13}$ and b) $Cu_{10}Co_2Sb_{4-y}As_yS_{13}$.

Fig. 9 Dimensionless thermoelectric figure of merit *ZT* as a function of temperature of the series a) $Cu_{12}Sb_{4-x}As_xS_{13}$ and b) $Cu_{10}Co_2Sb_{4-y}As_yS_{13}$.

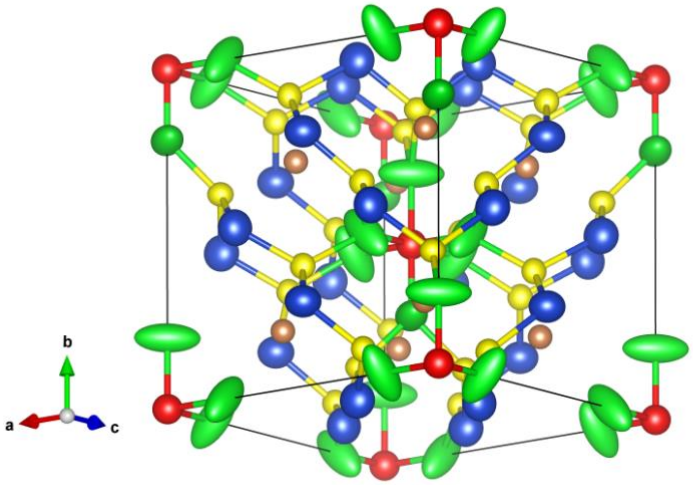

Figure 1

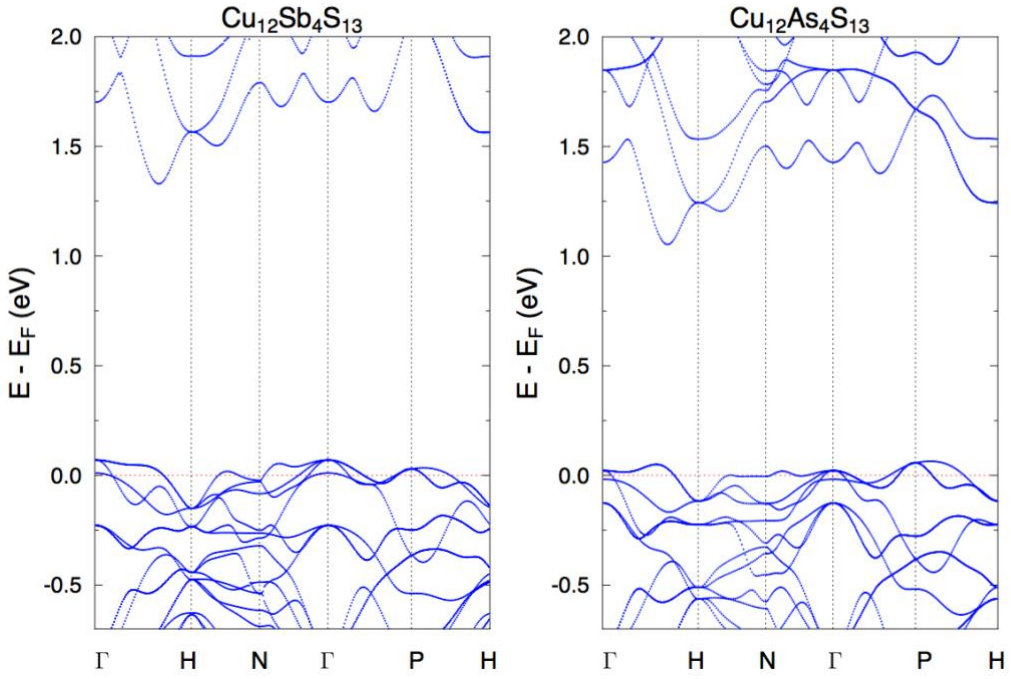

Figure 2

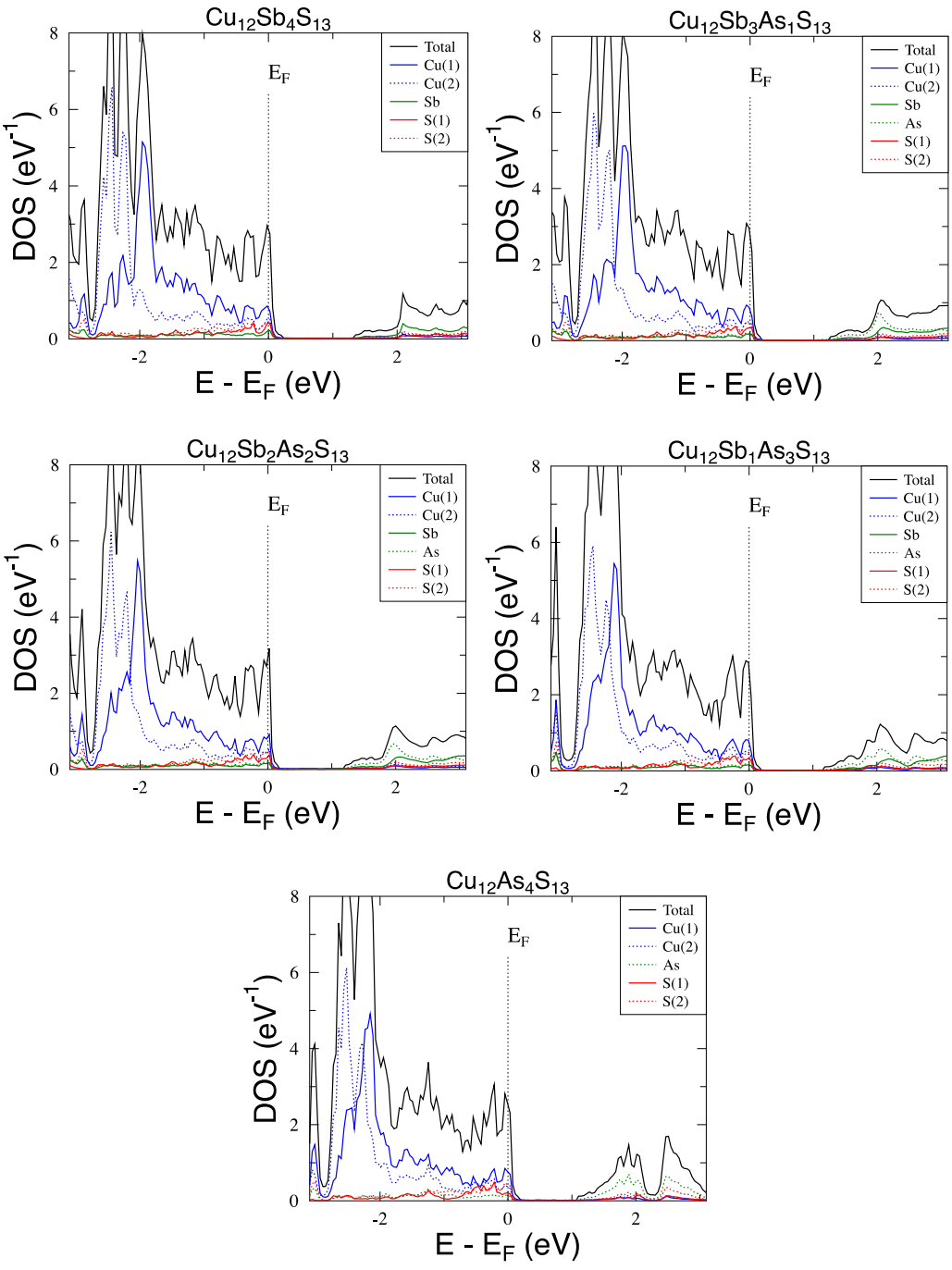
Cu12Sb4S13
Total
Cu(1)
Cu(2)
Sb
S(1)
S(2)
EF
DOS (eV-1)
E - EF (eV)
Cu12Sb3As1S13
Total
Cu(1)
Cu(2)
Sb
As
S(1)
S(2)
EF
DOS (eV-1)
E - EF (eV)
Cu12Sb2As2S13
Total
Cu(1)
Cu(2)
Sb
As
S(1)
S(2)
EF
DOS (eV-1)
E - EF (eV)
Cu12Sb1As3S13
Total
Cu(1)
Cu(2)
Sb
As
S(1)
S(2)
EF
DOS (eV-1)
E - EF (eV)
Cu12As4S13
Total
Cu(1)
Cu(2)
As
S(1)
S(2)
EF
DOS (eV-1)
E - EF (eV)

Figure 3

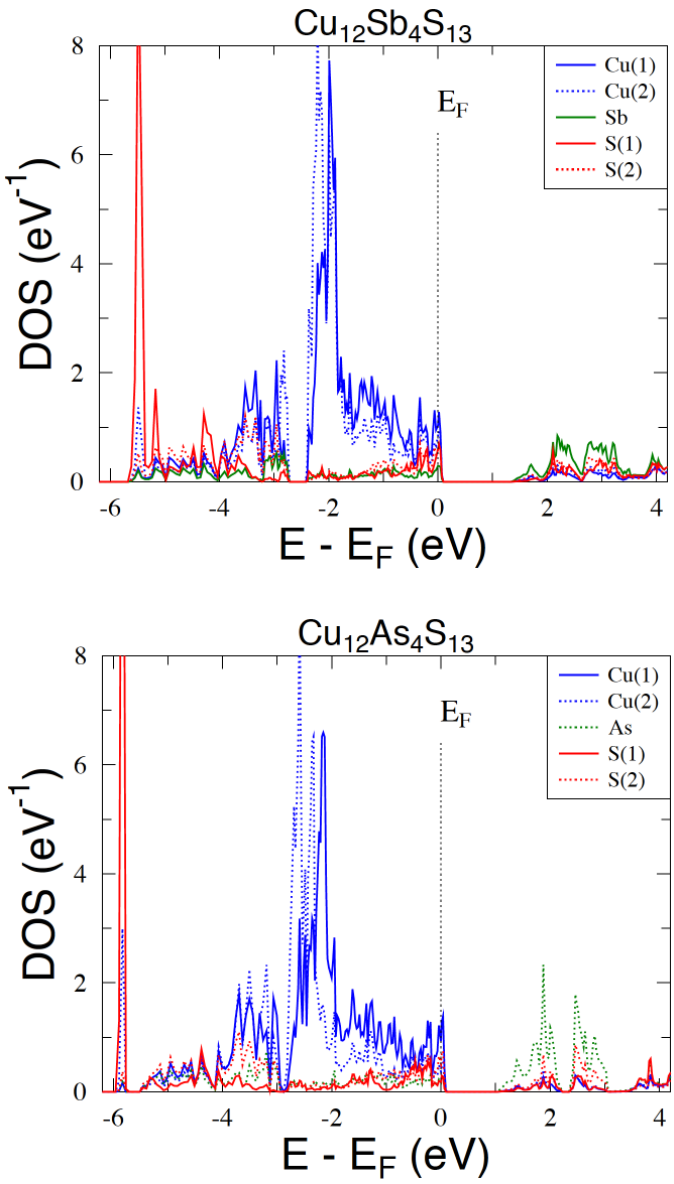
Cu12Sb4S13
Cu(1)
Cu(2)
Sb
S(1)
S(2)
EF
DOS (eV-1)
E - EF (eV)
Cu12As4S13
Cu(1)
Cu(2)
As
S(1)
S(2)
EF
DOS (eV-1)
E - EF (eV)

Figure 4

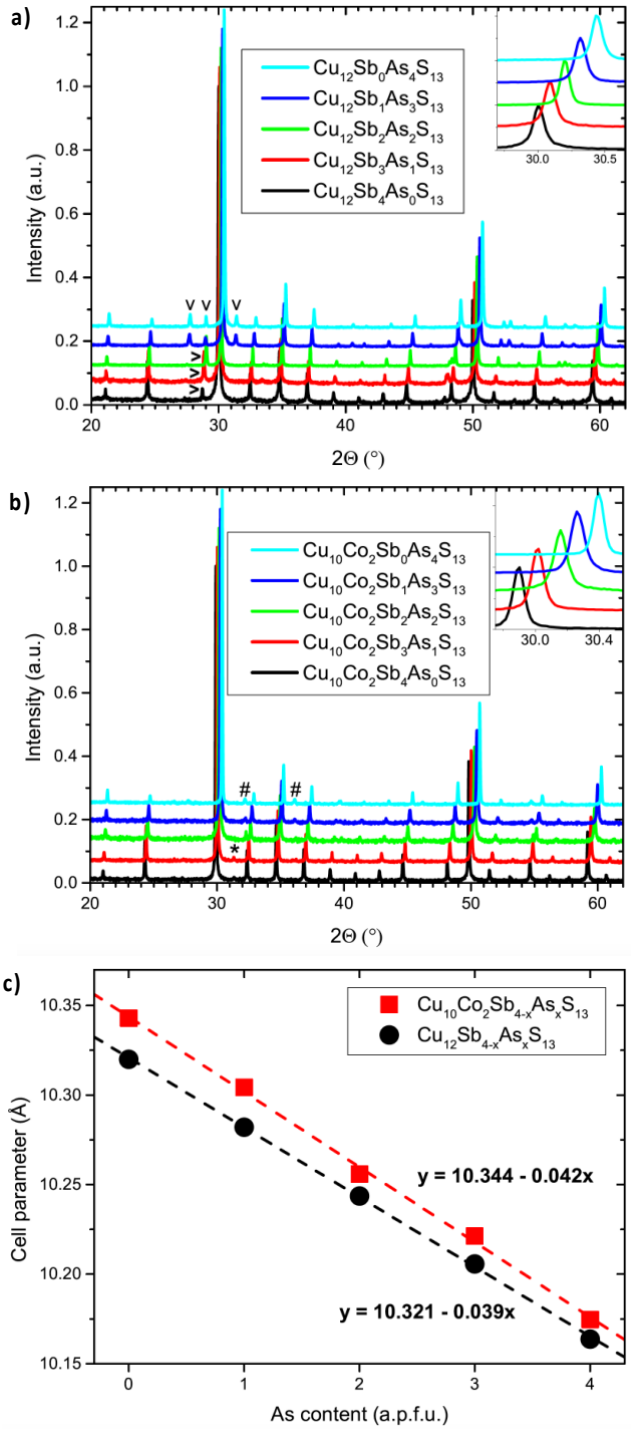
a)
Intensity (a.u.)
2Θ (°)
Cu12Sb0As4S13
Cu12Sb1As3S13
Cu12Sb2As2S13
Cu12Sb3As1S13
Cu12Sb4As0S13
b)
Intensity (a.u.)
2Θ (°)
Cu10Co2Sb0As4S13
Cu10Co2Sb1As3S13
Cu10Co2Sb2As2S13
Cu10Co2Sb3As1S13
Cu10Co2Sb4As0S13
c)
Cell parameter (Å)
As content (a.p.f.u.)
Cu10Co2Sb4-xAsxS13
Cu12Sb4-xAsxS13
y = 10.344 - 0.042x
y = 10.321 - 0.039x

Figure 5

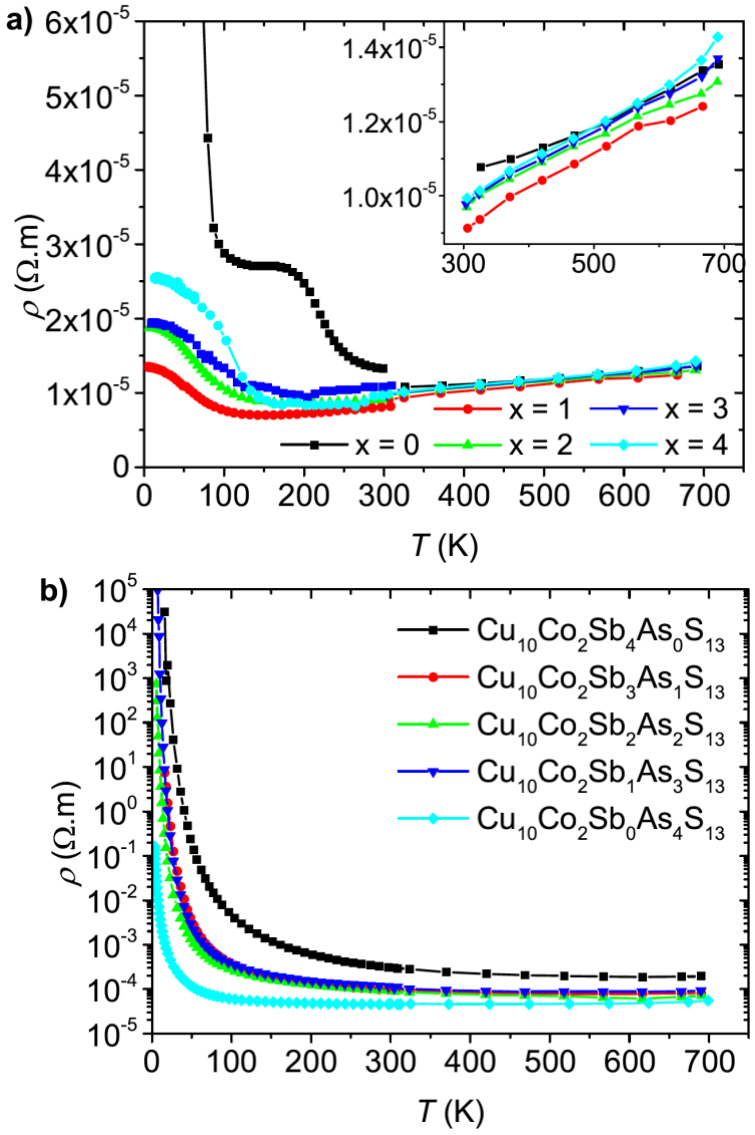
a)
6x10-5
5x10-5
4x10-5
3x10-5
2x10-5
1x10-5
0
ρ (Ω.m)
1.4x10-5
1.2x10-5
1.0x10-5
300
500
700
x = 0
x = 1
x = 2
x = 3
x = 4
0
100
200
300
400
500
600
700
T (K)
b)
ρ (Ω.m)
Cu10Co2Sb4As0S13
Cu10Co2Sb3As1S13
Cu10Co2Sb2As2S13
Cu10Co2Sb1As3S13
Cu10Co2Sb0As4S13
T (K)

Figure 6

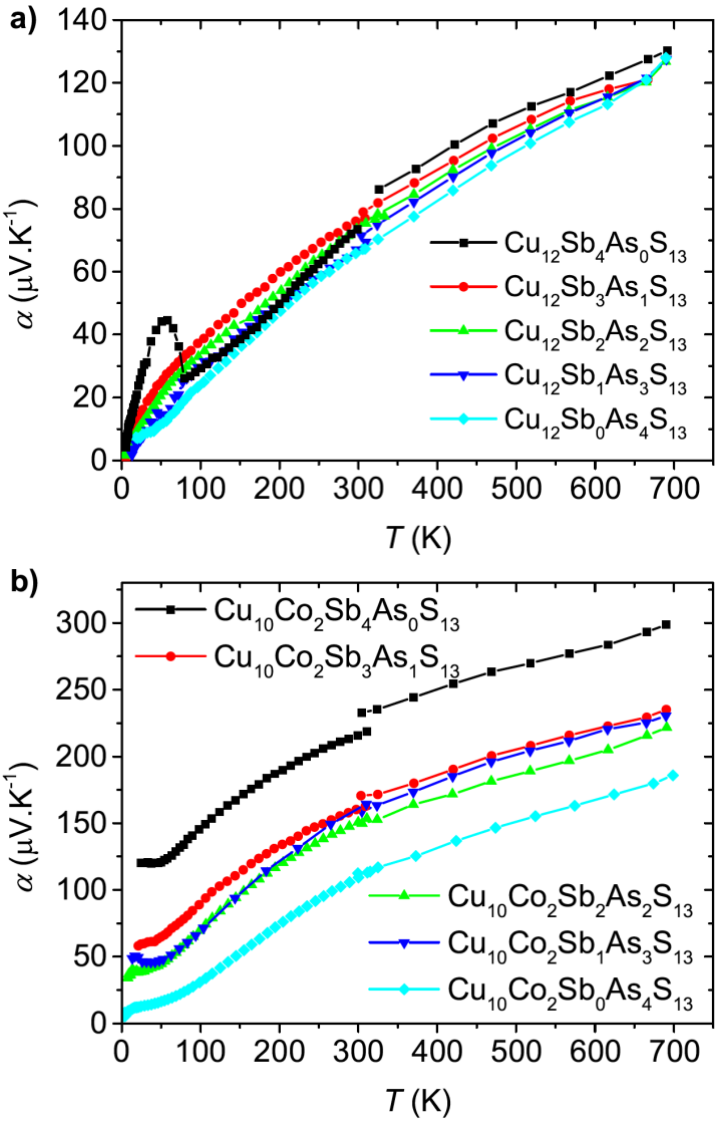
a)
α (μV.K⁻¹)
T (K)
Cu12Sb4As0S13
Cu12Sb3As1S13
Cu12Sb2As2S13
Cu12Sb1As3S13
Cu12Sb0As4S13
b)
α (μV.K⁻¹)
T (K)
Cu10Co2Sb4As0S13
Cu10Co2Sb3As1S13
Cu10Co2Sb2As2S13
Cu10Co2Sb1As3S13
Cu10Co2Sb0As4S13

Figure 7

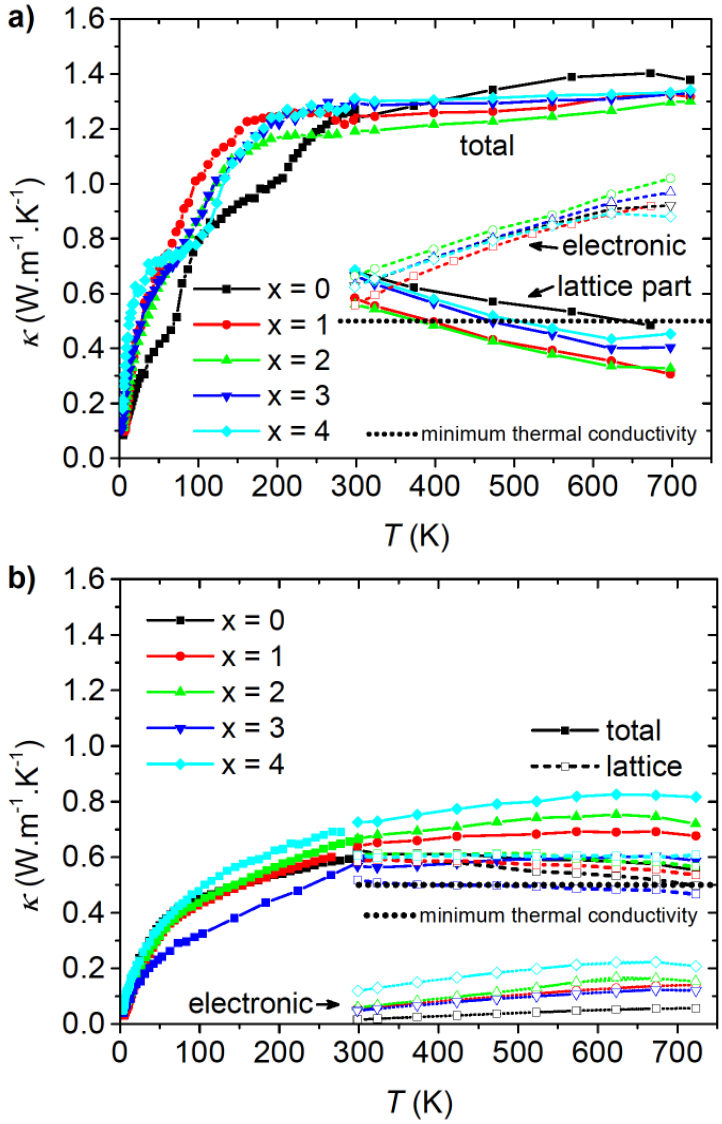
a)
b)
κ (W.m-1.K-1)
T (K)
total
electronic
lattice part
x = 0
x = 1
x = 2
x = 3
x = 4
minimum thermal conductivity
lattice

Figure 8

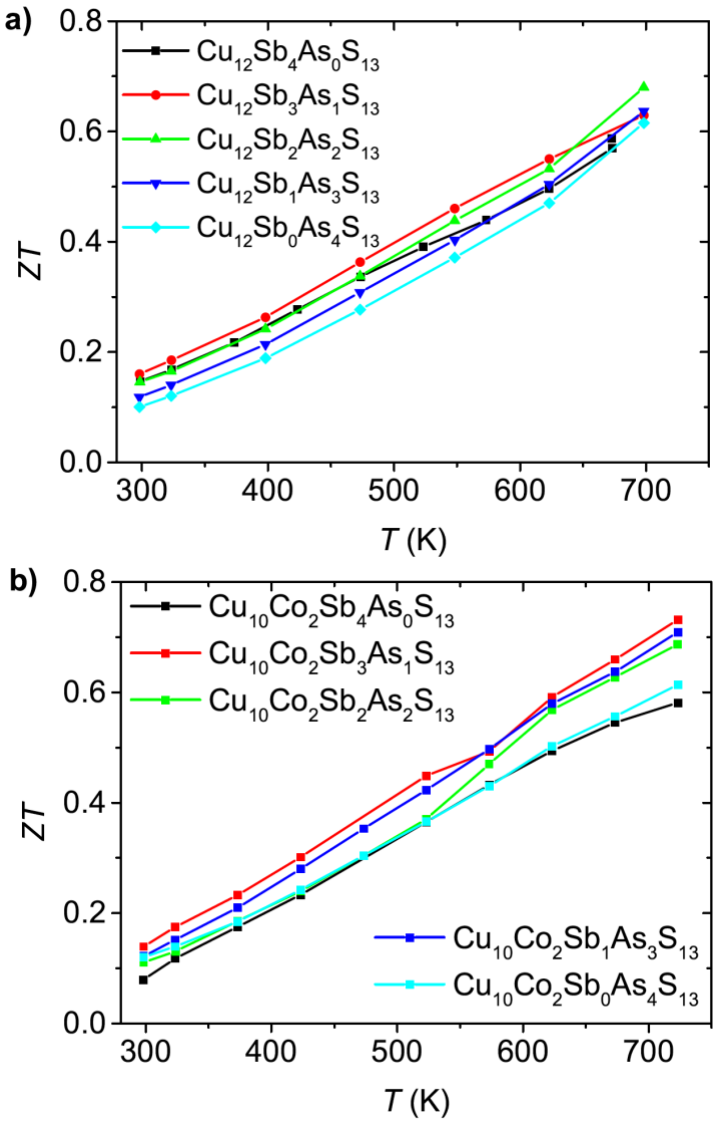
a)
0.8
0.6
0.4
0.2
0.0
ZT
300
400
500
600
700
T (K)
Cu12Sb4As0S13
Cu12Sb3As1S13
Cu12Sb2As2S13
Cu12Sb1As3S13
Cu12Sb0As4S13
b)
0.8
0.6
0.4
0.2
0.0
ZT
300
400
500
600
700
T (K)
Cu10Co2Sb4As0S13
Cu10Co2Sb3As1S13
Cu10Co2Sb2As2S13
Cu10Co2Sb1As3S13
Cu10Co2Sb0As4S13

Figure 9